ACS APPLIED NANO MATERIALS

www.acsanm.org Article

Sulfur Tolerant Subnanometer Fe/Alumina Catalysts for Propane Dehydrogenation

Lohit Sharma, Stephen C. Purdy, Katharine Page, Srinivas Rangarajan, Hien Pham, Abhaya Datye, and Jonas Baltrusaitis*

Cite This: https://doi.org/10.1021/acsanm.1c01366 Read Online

ACCESS | Metrics & More | Article Recommendations | Supporting Information

ABSTRACT: A series of Al_2O_3-supported Fe-containing catalysts were synthesized by incipient wetness impregnation. The iron surface density was varied from 1 to 13 Fe atoms/nm^2 spanning submonolayer to above-monolayer coverage. The resulting supported Fe-catalysts were characterized by N_2 physisorption, *ex situ* XRD, PDF, XAS, and AC-STEM and chemically probed by H_2-TPR. The results suggest that over this entire range of loadings, Fe was present as dispersed species, with only a very small fraction of Fe_2O_3 aggregates, at the highest Fe loading. The *in situ* sulfidation of Fe/Al_2O_3 resulted in the formation of a highly active and selective PDH catalyst. The highest activity with 52% propane conversion and ~99% propylene selectivity at 560 °C was obtained for the 6.4 Fe/Al_2O_3 catalyst, suggesting that this is the highest amount of Fe that could be fully dispersed on the support in sulfided form. XRD and AC-STEM indicated the absence of any crystalline iron sulfide aggregates after sulfidation and reaction. H_2-TPR results indicated that the amount of the reducible Fe sites in the sulfided catalyst remained constant above monolayer coverage, and increasing loading did not increase the number of reducible Fe sites. Consistent with these results, the reactivity per gram of catalyst showed no increase with Fe loading above monolayer coverage, suggesting that additional Fe remains conformal to the alumina surface.

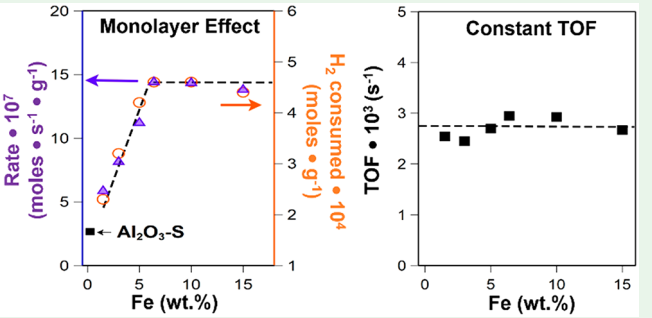

KEYWORDS: *Fe/alumina, propane dehydrogenation, Fe catalyst, alumina surface, sulfidation*

1. INTRODUCTION

The demand for alkenes, such as propylene, has increased by a 4% compounded annual growth rate during the past decade. It is further expected to increase in the upcoming years.[1−3] The nonoxidative dehydrogenation of propane (PDH) can selectively produce propylene from abundant natural gas resources.[4] During the PDH, activation of propane C−H bonds governs the overall catalytic performance. However, propylene, once formed, is more reactive than propane. This leads to further side reactions including cracking, deep dehydrogenation, and polymerization, typically resulting in low process selectivity and catalyst deactivation. Significant research efforts have focused on Cr and Pt alloys to achieve and sustain the activity of the catalysts as well as their selectivity and stability.[5] However, the high cost of Pt, its propensity to sinter at high temperatures, and its susceptibility to poisoning in the presence of sulfur compounds have led to research into catalyst material alternatives. In particular, there has been a growing interest in earth-abundant and environmentally benign catalytic materials, such as oxides of Fe, Cu, Co, Ga, Zn, V, Mo, Zr, and Sn, for selective dehydrogenation of propane.[6−15] However, these metal oxide-based catalysts (i) are not sufficiently active, (ii) suffer from low selectivity, (iii) rapidly deactivate with coke formation, and (iv) need their stability to be further improved.[5,16]

An alternative to improve the activity and selectivity is the addition of sulfur species over some PDH catalysts. For example, Resasco et al.[17] determined that when Ni/Al_2O_3 was treated with dimethyl sulfoxide, it exhibited improved selectivity and decreased coke formation during the isobutane (i-C_4) dehydrogenation. Wang et al.[18,19] have studied supported metals of Co, Cu, Mo, Mn, Zn, Fe on SiO_2 and determined that these H_2/H_2S pretreated catalysts exhibited higher propane selectivity. For example, the selectivity of about 87% was observed compared to 43% in the case of 13 Fe/SiO_2, and activity was 5 times higher than the corresponding oxide phase during i-C_4 dehydrogenation. A more recent work by Cheng and co-workers has investigated bulk and supported MoS_2 and showed that the rate of i-C_4 dehydrogenation over

Received: May 24, 2021

ACS Publications © XXXX American Chemical Society

https://doi.org/10.1021/acsanm.1c01366
ACS Appl. Nano Mater. XXXX, XXX, XXX−XXX

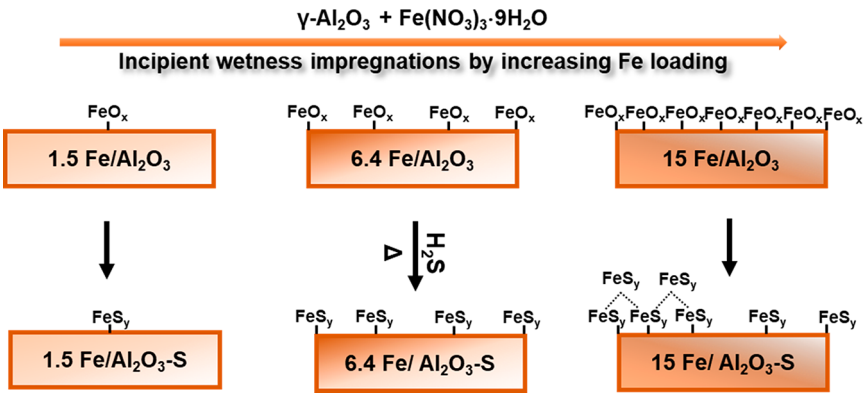

Figure 1. Schematic diagram showing the nature of the Fe subnanometer species in catalysts prepared via incipient wetness impregnation. After sulfiding, these dispersed Fe sites are active and selective for propane dehydrogenation, in the presence of H_2S.

the supported catalyst was ~7 times higher than over the bulk catalyst.[20] Recently, several studies examined the propensity and stability of a Fe-based catalyst for nonoxidative and oxidative PDH. For example, Fe-based catalysts (such as Fe/ZSM-5) were used for oxidative propane dehydrogenation.[21,22] Fe-based catalysts were also studied for nonoxidative propane dehydrogenation.[6,23,24] Lobo et al.[25] demonstrated that isolated Fe in a zeolite framework (Fe-ZSM-5) is an efficient PDH catalyst. A series of works by Li and co-workers[26,27] investigated the nonoxidative PDH over 20% $Fe/SO_4^{2-}/Al_2O_3$. It was proposed that the addition of the sulfur species as SO_4^{2-} was responsible for improved catalytic performance due to the electron-withdrawing effect of SO_4^{2-} species from metal ions.

Recently, Watanabe et al.[28,29] investigated SiO_2 supported Fe, Ni, and Co for PDH in the presence of H_2S. Their study showed that 20 Fe/SiO_2 after exposure to H_2S could selectively activate propane. The authors proposed that $Fe_{(1-x)}S$ was the active phase for the reaction based on XRD, XPS, and XAS techniques. These experiments were performed using the catalyst with a high fixed Fe metal loading of 20 wt % supported on SiO_2. At this Fe loading, the active catalytic phase can consist of Fe as monomers, oligomers, as well as crystalline FeS_x. It is generally accepted that at high loadings, Fe can result in 3d Fe_2O_3-like aggregates in oxide phase.[30] In contrast, Fe at low loadings leads to highly dispersed iron oxide clusters.[24,31,32] For example, it was determined that the catalytic activity during SCR is closely related to the number of Fe sites, particularly dispersed and oligomeric clusters,[31,32] whereas aggregated moieties reveal relatively low activity.[33] Presently, all the state-of-the-art work is performed at fixed Fe loading for the chemistry.[6,23−29] The catalytic behavior of dispersed and aggregated Fe species on supports for PDH has yet to be determined, especially in the presence of H_2S.

In this context, we have performed a systematic study of Fe loading over Al_2O_3 with incipient wetness impregnation. As shown in Figure 1, we find that the Fe species remain atomically dispersed, essentially in subnanometer form, over the entire range of Fe loadings we studied.

We explored the potential of Fe/Al_2O_3 as an earth-abundant and relatively inexpensive catalyst for propane activation in the presence of H_2S. In this study, we have synthesized catalysts with a known weight loading of Fe metal and determined their local atomic coordination to develop insights regarding the structure and the oxidation states. Further, the number of reducible iron species was determined using H_2-TPR. Here, we report that Fe/Al_2O_3 is very selective for propane dehydrogenation (>99% at 52% conversion at T = 560 °C and $C_3H_8:H_2:H_2S:N_2$ = 1.1:1:0.1:97.8) upon pretreatment with and cofeed of H_2S (especially 0.1 mol % cofeed), underlining the high activity-selectivity potential of the catalyst. This systematic study of Fe-based catalysts shows the vital role of dispersed Fe sites for the PDH chemistry. It will help design improved catalysts for PDH from a molecular perspective.

2. EXPERIMENTAL METHODS

2.1. Materials and Reagents. γ-Al_2O_3 (Sasol, Catalox SBA-150) was received from Sasol. 10 % H_2, 10% C_3H_8, and 1% H_2S (all diluted with N_2) were purchased from Airgas. $Fe(NO_3)_3·9H_2O$ and FeS were purchased from Acros Organics. Fe_3O_4 and Fe_2O_3 were purchased from Aldrich.

2.2. Catalyst Synthesis and Activation with H_2S for Propane Dehydrogenation Reaction. The γ-Al_2O_3 was calcined at 600 °C for 4 h under flowing air before impregnation. $Fe(NO_3)_3·9H_2O$ was dissolved in 0.5 M HNO_3 solution in DI water. The Fe/Al_2O_3 catalysts were prepared by incipient wetness impregnation of an aqueous solution of $Fe(NO_3)_3·9H_2O$ onto calcined γ-Al_2O_3 support. The impregnation step was performed under ambient conditions, and the impregnated mixture was stirred for ~30 min to maximize FeO_x dispersion. The catalyst was then dried overnight in ambient conditions. Later, the catalyst was dried with flowing air (1 L/min) at 120 °C for 4 h and calcined at 600 °C for 4 h under flowing air and a 1.33 °C/min ramp rate using a programmable furnace. The final synthesized catalysts are denoted as x Fe/Al_2O_3, where x is the weight percent of Fe impregnated on the support. Before the reaction, as synthesized x Fe/Al_2O_3 oxide catalysts were exposed to the stream of H_2S (P_{H_2S} = 0.01 atm, the balance N_2) at 600 °C for 4 h. Alternatively, the catalysts were pretreated in H_2 (P_{H2} = 0.01 atm, balance N_2) at 600 °C for 4 h. The calcined catalysts are referred to as x Fe/Al_2O_3 (e.g., 10 Fe/Al_2O_3 or 10 Fe), whereas H_2S pretreated catalysts are referred to as x Fe/Al_2O_3-S (e.g., 10 Fe/Al_2O_3-S or 10 Fe (S)). The H_2 pretreated catalysts are referred to as x Fe/Al_2O_3-H_2. Finally, if catalysts were characterized after one PDH cycle, they are referred to as x Fe/Al_2O_3-S1 (e.g., 10 Fe/Al_2O_3-S1 or 10 Fe (S1)).

2.3. N_2-Physisorption Studies. The surface areas of the catalysts were measured via nitrogen physisorption (−196 °C) using a Micromeritics ASAP 2020 instrument.[34] Pore size distributions were calculated using the Barret, Joyner, Halenda (BJH) model.[35]

2.4. Transmission Electron Microscopy (TEM). The air-exposed, powder samples were dispersed in ethanol and supported on holey carbon films on Cu grids for TEM. A JEOL NeoARM 200 CF microscope, operated at 200 kV, was used for this study. The spherical aberration corrector in this microscope provides a resolution of 0.71 Å. A JEOL dual EDS system using Oxford AZTEC software was used for elemental analysis via X-ray fluorescence in the TEM. Images using a 30 μm condenser aperture and 8 cm detector camera

https://doi.org/10.1021/acsanm.1c01366
ACS Appl. Nano Mater. XXXX, XXX, XXX−XXX

length in annular dark field (ADF) mode images were recorded simultaneously with annular bright field (ABF) images.

2.5. X-ray Diffraction (XRD). The powder XRD and X-ray pair distribution function (PDF) measurements were performed at the PDF beamline (ID-28-1) of the National Synchrotron Light Source II. Samples were loaded into 1 mm OD Kapton tubes and sealed at both ends with epoxy. Measurements were made using an X-ray wavelength of 0.166 35 Å and a PerkinElmer large area detector. The sample to detector distance for XRD and PDF measurements was 240 and 840 cm, respectively. For both distances, a CeO_2 standard was used for detector calibration.

Detector calibration, 2D pattern masking, and 2D pattern integration were performed using DIOPTAS software.[36] The reduced pair distribution function, $G(r)$, was extracted from $I(q)$ data using the program PDFgetx3.[37] A q range of 0.9−23.0 $Å^{-1}$ was used for all samples for the Fourier transform, and the R_{poly} value was set to 0.9. Background subtraction was done using a scan of an empty polyimide capillary. Small box simulation of PDF data was done using PDFgui software.[38]

2.6. X-ray Absorption Spectroscopy. X-ray absorption spectroscopy at the iron K edge (7110.7 eV) was performed at the MRCAT bending magnet line (10-BM) of the Advanced Photon Source, Argonne National Laboratory.[39] Catalysts for XAS were ground into a fine powder and pressed into a self-supporting pellet. Catalysts were mounted in a nylon washer and secured with Kapton tape. Measurements were performed in fluorescence mode using a vortex 4 element detector. The monochromator energy was calibrated using the inflection point of iron foil, with the absolute energy taken from literature.[40] Scans were taken in step scanning mode over an energy range of 6910−7657 eV, giving a k-max of 11.8 $Å^{-1}$. Each catalyst was scanned 3 times and averaged to give the analyzed spectra.

Data reduction and analysis were performed using the Demeter software suite. The edge energy was taken as the first derivative maximum of the rising edge of the X-ray absorption near edge structure (XANES). The pre-edge energy was taken as the point of maximum intensity (first derivative zero) of the pre-edge peak. The absolute energy resolution of the monochromator (Si 111) at the Fe K-edge is 0.8 eV (1×10^{-4} $\Delta E/E$), and the sample-to-sample variation in energy was better than 0.1 eV. Self-absorption artifacts were removed using the FLUO algorithm implemented in Athena.[41] The nominal composition of the catalyst and the sample to beam angle (45°) were used as inputs for the correction. Normalization was performed using a first-order polynomial for the pre-edge (−200 to 30 eV) and a third-order polynomial for the postedge (125 to 535 eV). Bare atom absorption was subtracted using a spline fit over the entire measured k range and using an R_{bkg} value of 1.0. Extended X-ray absorption fine structure (EXAFS) fitting was performed in R-space over a k-range of 2.7−11.0 $Å^{-1}$ and an R range of 1.0−3.0 Å, giving 10 free parameters. All models used fewer free parameters than were available based on Nyquist theorem.

Models were constructed using a bulk crystallographic reference of Fe_2O_3. All paths shared an E_0 correction, and all bond distances were correlated through an isotropic lattice expansion coefficient ε, where the bond distance for each path was defined as

$$R = R_{eff}(1 + \varepsilon) \quad (1)$$

For samples with Fe−Al scattering, the Fe_2O_3 FEFF input file generated by Artemis was modified by replacing neighboring Fe atoms with Al. The first shell oxygen scattering was fit using two separate oxygen paths sharing a single Debye−Waller factor. Similarly, the second shell was fit using two Fe−Al single scattering paths with a single Debye−Waller factor. Each path was given a separate coordination number. Allowing for separate Debye−Waller factors for each oxygen path did not significantly improve fit statistics or change the fit coordination numbers for each path. The amplitude reduction factor S_0^2 for all samples and paths was fixed to the value fit iron foil using a bulk BCC Fe model. Full details of the Fe foil fit are given in the Supporting Information.

2.7. H_2 Temperature-Programmed Reduction (H_2-TPR). H_2-TPR was performed using the same steady-state reactor used for kinetic studies equipped with an MKS Cirrus 2 mass spectrometer. ~75 mg of the catalyst was loaded into the reactor and pretreated at 300 °C for 1 h with a 20 °C/min ramping rate under 30 mL/min 2% O_2/N_2 flow for the as-synthesized catalyst (non-H_2S-treated). After cooling down to 30 °C in N_2, N_2 was replaced with 2% H_2/N_2 at 25 mL/min for 15 min. In the following step, the temperature was ramped to 800 °C at 10 °C/min in 2% H_2/N_2. The sulfided catalyst was prepared by pretreating at 600 °C for 4 h in 1% H_2S/N_2. Subsequently, the catalyst was flushed in N_2 for 15 min. After cooling down to 30 °C in N_2, 2% H_2/N_2 was flowed at 30 mL/min for 15 min. In the following step, the temperature was ramped to 800 °C at 10 °C/min in 2% H_2/N_2 flow. The calibrated H_2-TPR was utilized to calculate the number (moles) of H_2 consumed. For calibration, at least four different CuO amounts were utilized to determine the number of H_2 atoms consumed.[42] The standard error was estimated to be about 4% based on the calibration curve obtained using CuO, Fe_2O_3, and Fe_3O_4 standards. It was observed that catalyst after H_2S pretreatment resulted in the evolution of H_2S during H_2-TPR (Fe-S + H_2 → Fe + H_2S). Concurrently, the number of H_2 molecules consumed was calculated and used to determine the number of reducible Fe present on the surface, assuming H_2:Fe was 1:1.

2.8. Steady-State Catalytic Reactivity Testing. The steady-state kinetic experiments were performed in a quartz tube reactor (6.8 mm i.d.). All reported steady-state experiments were carried out using either 200 mg or 30 mg of catalyst, with the reactor operating at 1 atm with negligible pressure drop. Quartz wool was placed in the reactor to support the catalyst bed. The temperature was ramped at 20 °C/min to 600 °C. Typically, the catalyst was pretreated in a stream of H_2S (P_{H_2S} = 0.01 atm, the balance N_2) at 600 °C for 4 h. More details regarding the experimental setup can be found in the previous work.[43,44] The number of reducible [Fe] sites was determined using H_2-TPR. The rate (based on C_3H_8 conversion per second per gram of catalyst) and selectivity were calculated according to eqs 2−6. The reaction rate represented is multiplied by 10^7, and the conversion is extensively reported in the Supporting Information.

$$\text{rate}\left(\frac{\text{mol}}{\text{g·s}}\right) = \left[\text{conversion} \times \text{inlet concentration}\ (C_3H_8) \times \text{flow rate}\left(\frac{\text{mL}}{\text{min}}\right) \times \left(\frac{1}{60}\frac{\text{min}}{\text{s}}\right) \times \left(\frac{1}{1000}\frac{\text{L}}{\text{mL}}\right)\right]\left[\frac{1}{\left(22.4\frac{\text{L}}{\text{mol}}\right) \times \text{loading weight (g)}}\right] \quad (2)$$

$$\text{selectivity}\ (\%) = \frac{[C_3H_6]_{out}}{[C_3H_8]_{in} - [C_3H_8]_{out}} \times 100 \quad (3)$$

$$\text{conversion}\ (\%) = \frac{[C_3H_8]_{in} - [C_3H_8]_{out}}{[C_3H_8]_{in}} \times 100 \quad (4)$$

$$\text{TOF}\ (s^{-1}) = \frac{\text{rate}}{\text{number of reducible sites [Fe]}} \quad (5)$$

$$F/I = \frac{\text{final reaction rate (TOS = 10 h)}}{\text{intial rate (TOS = 5 min)}} \quad (6)$$

The carbon balance for the reaction was 100% within experimental error. The reaction temperature of 560 °C was selected for the study. A low concentration of C_3H_8 (1.1 mol %) was used to conduct experiments safely to reduce the flow and concentration of H_2S in the cofeed while maintaining the C_3H_8:H_2S (1:0.1) ratio in the reactant stream.[45] This is consistent with the literature where propane dehydrogenation reactions are carried out between 450 and 650 °C

https://doi.org/10.1021/acsanm.1c01366
ACS Appl. Nano Mater. XXXX, XXX, XXX−XXX

with C_3H_8 feed concentration varying from 1.5 to 20 mol %.[1] The first data point was collected after 5 min time-on-stream (TOS) under given reaction conditions. Replicate experiments reproduced reaction rates within ±5%, and selectivity can be reproduced within ±2%. The reaction studies typically were performed using N_2 dilution (1.1% C_3H_8, 97.8% inert (N_2), 1% H_2, and 0.1% H_2S). Therefore, the mole change during the reaction was ignored, and it was assumed that the volumetric flow rate remains constant.[46] High conversion data were obtained using 200 mg catalyst and a total volumetric flow rate of 50 mL/min. The catalyst amount was reduced to 30 mg to obtain data under differential conditions. The total volumetric flow rate was also increased to 75 mL/min. At the same time, the gas composition was maintained as indicated above by adjusting the flow rate. The catalyst was uniformly mixed with 150 mg of sand. The thermal conversion was low (<0.1%). However, at low conversion, the moles of CH_4 and C_2H_4 formed due to gas phase reaction were comparable. The selectivity value has been corrected for background contributions from thermal cracking of propane, as measured over sand under the same conditions. At 560 °C, propane conversion due to cracking amounts to 0.1% and is ~60% selective to propene. At the end of the reaction, the catalyst was purged, cooled to room temperature under N_2, removed from the reactor, and stored in a glass vial for spectral characterization.

3. RESULTS

3.1. Catalyst Textural Property Characterization. N_2 sorption has been used to measure the textural properties of the as-synthesized catalysts. The N_2 adsorption−desorption isotherms shown in Figure S1a followed type IV isotherms with distinct hysteresis loops indicating their mesoporosity which are observed when monolayer and multilayer adsorption of N_2 occurs.[47] Increasing the Fe loading led to a continuous decrease in the BET surface area. The loss of surface area can be explained by a conformal layer of the Fe species which only add weight to the catalyst but do not increase the physical surface area. The loss of pore volume is likewise consistent with this picture, since the pore sizes remained unchanged with Fe loading as shown in Figure S1b.[35] The formation of second feature around 8 nm at the highest weight loading is consistent with the likely presence of a small fraction of Fe_2O_3 aggregates (resulting in pore blocking), as we show later. The corresponding surface area, pore volume, pore size, and the Fe loading (atoms·nm^{-2}) are summarized in Table 1.

3.2. Powder X-ray Diffraction (XRD) and X-ray Pair Distribution Function (PDF). Synchrotron XRD patterns were used to analyze the phase composition of the as-synthesized catalysts, and the bare γ-Al_2O_3 support is shown in Figure 2. Peaks characteristic of γ- Al_2O_3 are seen, and no contribution from other crystalline phases is evident. Diffraction peaks in the patterns associated with the aluminum sublattice, (111), (220), (311), and (222), are broadened and asymmetric due to antiphase and rotational boundaries, while the well-ordered oxygen sublattice peaks (400) and (440) are sharper and more symmetric.[48] As Fe loading is increased, several of the broad asymmetric peaks increase in intensity relative to the oxygen lattice peaks. This is attributed to iron adsorption onto different surface planes of alumina, which modifies the structure factor of their respective Bragg peak. Note that despite the increase in structure factor for the aluminum sublattice peaks, there is no peak shift, which suggests that iron is not incorporated into the bulk of Al_2O_3. These results suggest that iron species on alumina are only ordered over a very short-range at all loadings. Subsequently, nonsynchrotron XRD was also utilized to study the as-synthesized form, and the spent catalyst and the results are discussed in Figure S2. The diffraction peaks related to the Fe_2O_3 crystalline phase were absent even for the highest loading of 15% Fe, indicating either an amorphous nature or dispersed state with no long-range order.[49] TEM results confirm this picture and show that there are no detectable crystalline phases other than alumina (Figures S3, S4, and S5). The STEM ADF images are ideal for detecting the presence of the heavier element (Fe) on the lighter Al_2O_3 support. While higher contrast regions were seen, they did not reveal any lattice fringes corresponding to iron oxides. The only crystalline phase detected was γ alumina. The EDS map (Figure S6) shows that Fe is well dispersed even in the 15 wt % Fe sample. Some regions show higher concentration of Fe. These regions, however, do not yield any lattice fringes corresponding to iron oxides, so we infer that they could be due to amorphous or poorly crystallized Fe oxide. The absence of any visible large particles confirms that the Fe is well dispersed, even on the 15 wt % Fe sample. This sample was also studied in its sulfided form (Figures S7−S9) showing very similar structure; i.e., Fe is well dispersed while EDS confirms the sample is sulfided.

To gain further insight into the local iron structure, a locally sensitive technique, pair distribution function was measured on the catalysts. The X-ray pair distribution functions (PDFs) of Fe/Al_2O_3 catalysts and the bare Al_2O_3 support are plotted in Figure S10a. Below 8 Å, the series shows several peaks that have changed in intensity relative to the bare support, whereas at longer length scales, the patterns only show minor variation. This result is in line with the XRD results showing only

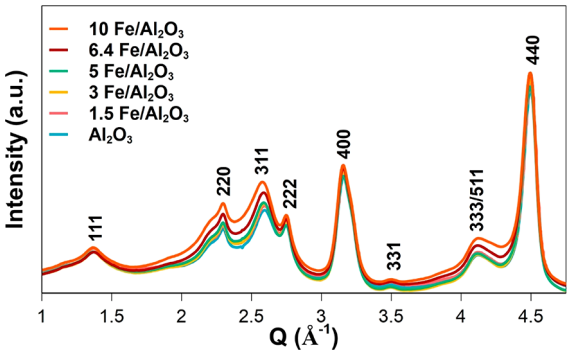

Figure 2. Synchrotron XRD patterns of Fe/Al_2O_3 catalysts. Fe/Al_2O_3 represents as-synthesized catalyst after calcination in air at 600 °C for 4 h.

Table 1. Summary of Textural Properties of Various Fe Loading (wt %) over Al_2O_3 after Calcination in Air at 600°C for 4 h

catalyst	surface area[a] (m^2/g)	pore volume (cm^3/g)	pore size (nm)	Fe loading (atoms·nm^{-2})[b]
Al_2O_3	142	0.45	15	0
1.5 Fe/Al_2O_3	142	0.45	15	1.14
3 Fe/Al_2O_3	140	0.42	15	2.28
5 Fe/Al_2O_3	138	0.41	8,15	3.91
6.4 Fe/Al_2O_3	134	0.38	8,15	5
10 Fe/Al_2O_3	132	0.37	8,15	8.17
15 Fe/Al_2O_3	120	0.31	8,15	13.26

[a]The surface area is based on the BET method. Pore size is based on the BJH method. [b]Values for Fe loading (atoms·nm^{-2}) were estimated on the assumption that all Fe is fully dispersed over Al_2O_3.

https://doi.org/10.1021/acsanm.1c01366
ACS Appl. Nano Mater. XXXX, XXX, XXX−XXX

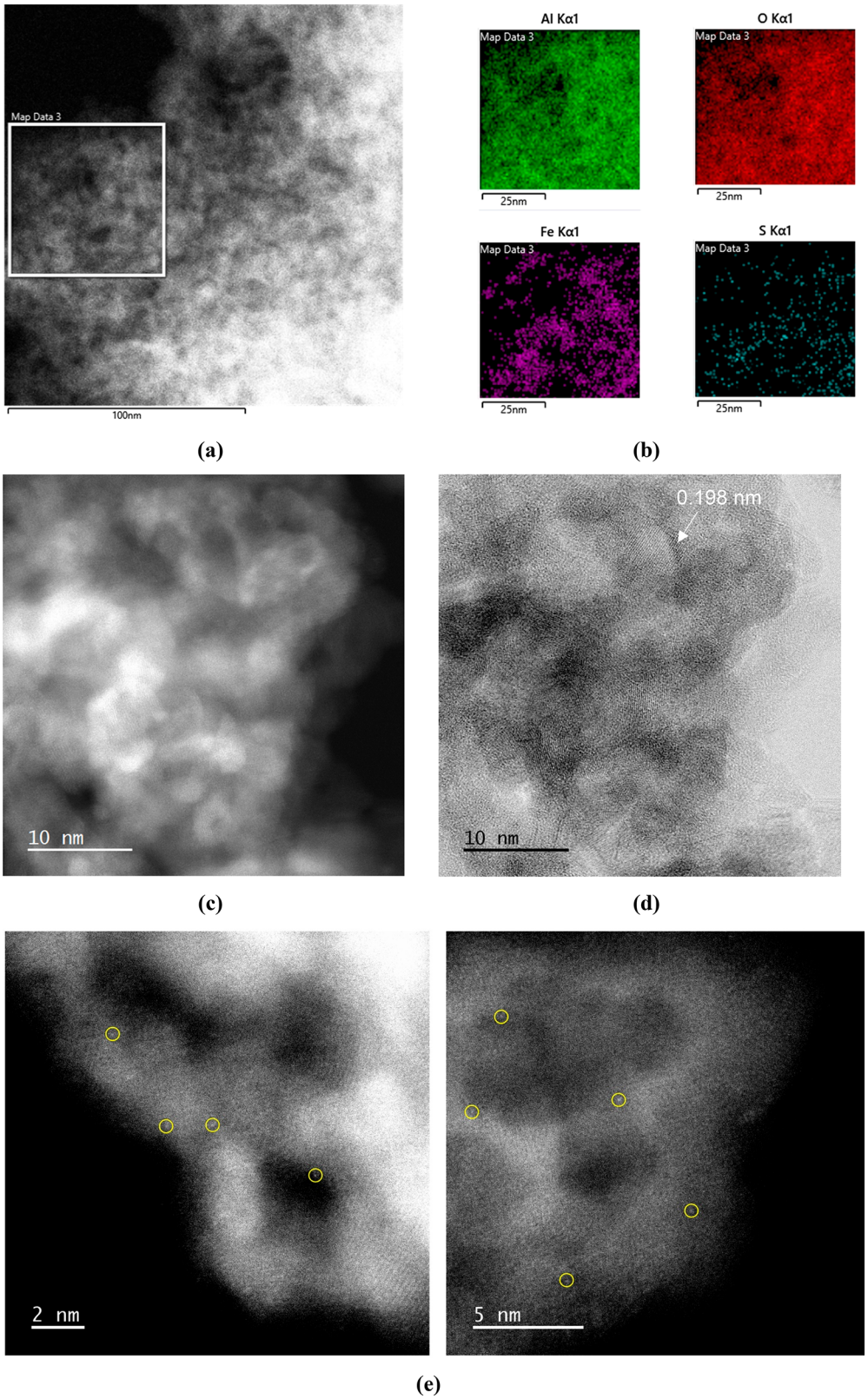

Figure 3. (a) ADF image of the spent 6.4 Fe/Al_2O_3-S1 sample after sulfiding and one cycle of PDH. (b) The EDS map of the region in the box shows Fe and S are well dispersed and no distinct Fe nanophases are visible in the image. (c) ADF image and (d) ABF image of the 6.4 Fe/Al_2O_3-S1 sample after one cycle of PDH. While regions of higher contrast are seen via ADF, they are not associated with any Fe containing crystalline phases. The prominent visible lattice fringes come from alumina, in this case the (400) reflection from γ alumina, with a *d*-space of 0.198 nm. (e) Higher magnification ADF images of the 6.4 Fe/Al_2O_3-S1 sample after one cycle of PDH. We observe single Fe atoms, as indicated by the yellow circles.

https://doi.org/10.1021/acsanm.1c01366
ACS Appl. Nano Mater. XXXX, XXX, XXX−XXX

changes in the relative intensity of a subset of diffraction peaks and the diffuse scattering background. The changes in relative intensity are due to scattering pairs involving iron, which due to having a higher X-ray atomic form factor, leads to higher intensity peaks. To determine whether the local Fe structure is better represented by substitution of alumina or by a subnanometer sized iron oxide phase, a difference analysis was performed by subtracting the scaled Al_2O_3 pattern from each Fe/Al_2O_3 catalyst.

Figure S10b shows the difference patterns for Fe/Al_2O_3 catalysts. The Fe loading for 1.5 Fe/Al_2O_3 was too low to produce a difference spectra signal above the noise and hence was not included. The residual peaks left after the difference represent the modification of the support due to Fe loading. Qualitatively, this allows the determination of the coherent length scale of iron species on the catalyst. Looking at the first 5 Å, the largest residual peaks align well with the local structure of Fe_2O_3, which suggests that iron has not substituted into the Al_2O_3 structure but rather is present as subnanometer surface Fe_2O_3 species. Past 5 Å, the Fe_2O_3 and difference patterns do not match, which suggests that the length scale of iron species on the support is on the order of 1−2 coordination polyhedra. Residual signal not associated with the iron structure reflects subtle structural changes of the Al_2O_3 support, the features of which appear highly similar in all samples.

Previously, Xie et al.[50] suggested that iron oxides form a monolayer on the γ-Al_2O_3 surface. They reported a Fe loading threshold of 0.052 g Fe_2O_3 per 100 m^2 Al_2O_3 or ∼4 Fe atoms nm^{-2} to form monolayer coverage. Of note, the authors also estimated the theoretical coverage of 0.13 g per 100 m^2 Al_2O_3 or ∼11 Fe atoms nm^{-2} to form monolayer coverage. Similarly, other studies also suggested that iron can be dispersed between 4 and 5.5 Fe atoms nm^{-2} over γ-Al_2O_3 support.[30,51] Accordingly, the XRD and PDF results in this work indicate the possibility of forming a highly dispersed Fe-phase. Notably, temperatures higher than 1000 °C are usually required to form aluminate spinel ($FeAlO_3$) or crystalline hercynite ($FeAl_2O_4$) from Fe_2O_3 and Al_2O_3.[52,53] The XRD patterns of the Fe/Al_2O_3-S1 catalysts after one complete PDH cycle (Figure S2d) with H_2S cofeed were also acquired. Similar to the fresh catalysts, no diffraction peaks for crystalline phases other than γ-Al_2O_3, such as FeS_x,[54] were observed. The results indicate the lack of any bulk like FeS_x species. Of note, the spent catalyst was exposed to air before the examination, which may result in partial oxidation of the catalyst. The 6.4 Fe catalyst was also studied via AC-STEM after one reaction cycle of PDH. While regions of higher contrast are seen in the EDS map (Figure 3), there is no corresponding crystalline phase detected in the images, the only crystalline structures observed correspond to the alumina as seen in the higher magnification images. Higher magnification images show contrast ascribed to single atoms of Fe, confirming that the Fe remains atomically dispersed in this sample after reaction. These catalysts were also air exposed, but EDS shows evidence for Fe and S (Figures S8 and S9). After recording images from 50 regions of this sample, we found only one that contained a crystalline Fe particle (Figure S11). While not representative of the sample as a whole, this image demonstrates that such species would be readily visible in the AC-STEM images, since the microscope resolution is 0.71 Å. These results confirm the absence of any crystalline Fe phases in the spent catalyst.

3.3. X-ray Absorption Spectroscopy To Determine the Structure of the As-Synthesized Catalyst.

Figure 4a shows the Fe K-edge XANES for the series of Fe/Al_2O_3 catalysts with increasing Fe loading. XANES edge energies and pre-edge peak positions for Fe_2O_3 reference and Fe/Al_2O_3 catalysts are tabulated in Table S1. The edge energy and pre-edge peak position did not vary significantly with Fe loading, with the pre-edge peak position being 7113.2 eV and the edge position being 7121.5 eV. This edge position and pre-edge peak were close in value to Fe_2O_3, consistent with the Fe^{3+} oxidation state for all catalysts. The pre-edge peak position of the catalysts is shifted to slightly lower energy and is different in shape compared to the Fe_2O_3 reference, and this is likely due to a difference in point group symmetry of the absorber. Across the loading series, there were systematic changes in the intensity in the pre-edge region. The pre-edge peak intensity increased with Fe loading, and in the region between the pre-edge peak maximum and the main edge, the intensity systematically increased with Fe loading. This trend has previously been documented in dispersed Fe on Al_2O_3 and was attributed to the formation of extended iron oxide species, and the current results are consistent with this interpretation.[30] On the basis of the surface area of Al_2O_3 used in this study, monolayer coverage of iron is expected to be reached at a Fe loading of 6.4 wt %; however, the intensity increase between 7115 and 7118 eV appears to increase proportionally with loading rather than abruptly when Fe loading surpasses monolayer coverage. The gradual trend can be rationalized through the formation of a minority species of crystalline Fe_2O_3 or 2D/oligomeric iron oxide species, both of which would allow for Fe−Fe orbital hybridization responsible for the intensity increase, consistent with STEM results.[55] As the fraction of iron atoms with a nearby iron atom nearby increases, the XANES intensity between 7115 and 7118 eV increases.

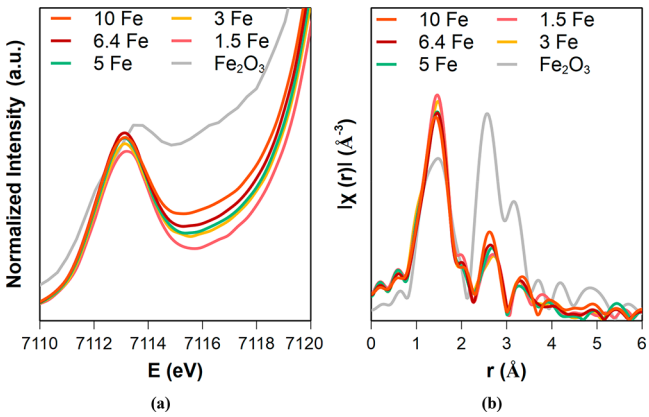

Figure 4. *Ex situ* (a) Fe K edge XANES and (b) *R* space EXAFS magnitude of as-synthesized 1.5−10 Fe/Al_2O_3 catalysts.

Figure 4b shows the *R*-space EXAFS spectra Fe/Al_2O_3 catalysts with increasing Fe loading and reference spectra of Fe_2O_3. Fe_2O_3 has three distinct peaks in the local structure seen by EXAFS corresponding to its immediate oxygen environment (1.5 Å phase uncorrected distance) and its second and third nearest neighbor iron atoms (2.7 and 3.2 Å phase uncorrected distance). In contrast, the Fe/Al_2O_3 catalysts have a more symmetric Fe−O scattering peak and a weak second shell peak. As iron loading increases, the Fe−O scattering peak decreases in intensity, and the second shell peak increases in intensity. On the basis of the qualitative trends, a model was constructed for the catalysts using the local

https://doi.org/10.1021/acsanm.1c01366
ACS Appl. Nano Mater. XXXX, XXX, XXX−XXX

environment of Fe_2O_3 with Al as the second nearest neighbor. Fitting results are summarized in Table S2.

Two models were tested for the first shell Fe−O scattering in 1.5 Fe/Al_2O_3, having either one or two Fe−O paths, with results shown in Figure S12 and Table S3. Including a second Fe−O path with a longer bond distance improved the *r*-factor and reduced χ^2 value of the fit and was then used to model the entire series. Several trends emerged from the fitting results. First, the total Fe−O coordination for the Fe/Al_2O_3 catalysts was about 5, except for 10 Fe/Al_2O_3, which was closer to 6. Unlike Fe_2O_3, the number of short Fe−O bonds and the number of long Fe−O bonds were not equal, instead having four short bonds (1.92−1.94 Å) and one long bond (2.09−2.11 Å). A previous report on Fe/Al_2O_3 EXAFS similarly modeled one short and one long Fe−O bond distance and obtained similar Fe−O coordination numbers reported here.[30] For the short Fe−O bond, the coordination number decreased from 3.9 to 3.3 as Fe loading was increased from 1.5 to 6.4%. The long Fe−O bond also showed small variation between the catalysts (0.9−1.3) though the change was not systematic. The trend in the total Fe−O coordination number could reflect multiple sites of iron adsorption on the Al_2O_3 surface with different oxygen environments that are filled progressively as the Fe loading is increased.

The EXAFS magnitude of the second nearest neighbor of the Fe/Al_2O_3 catalysts is similar in position to that of Fe−Fe scattering in Fe_2O_3 at 2.7 Å (phase uncorrected distance). Examinination of the imaginary component of the catalyst (Figure S13 and Table S4) and the *Q* space real component of the peak (Figure S14) suggests a lighter scatter such as aluminum. The total Fe−Al coordination number varied between 2 and 3 among both paths. The lack of Fe−Fe coordination in the second shell of catalysts with Fe loading below 6.4% confirms that most Fe is present as single (or dispersed) sites in these catalysts. The short Fe−Al path coordination number varied from 0.6 to 0.9, and the long path varied from 1.2 to 2.3. This suggests that 2−3 of the oxygen bonds to iron come from bonding with the support, while the remaining (1−2) Fe−O bonds come from an adsorbate or ligand, such as a hydroxyl group or water. EXAFS fittings for Fe foil and Fe/Al_2O_3 catalysts are shown in Table S5 and Figures S15−S20.

In line with the monolayer iron coverage predictions, the 10 Fe/Al_2O_3 catalyst could not be modeled using aluminum second nearest neighbors. Instead, a model using Fe−Fe scattering from Fe_2O_3 was used to model the EXAFS. In addition to the Fe−Fe coordination numbers being lower than that of the bulk oxide, the iron environment around the absorber is quite distorted relative to that of bulk Fe_2O_3. In bulk α-Fe_2O_3, iron has Fe neighbors at 2.899 Å (1 neighbor), 2.968 Å (3 neighbors), and 3.361 Å (3 neighbors). In contrast, 10 Fe/Al_2O_3 was fit with 0.9 neighbors at 3.03 Å and with 2.3 neighbors at 3.56 Å. The lengthening of the Fe−Fe bonds relative to Fe_2O_3 is indicative of lattice expansion. This phenomenon is common in nanoscale oxides, as the diminishing Madelung potential near the oxide surface causes the lattice to expand.[56] While the Fe−O bond distances are in line with Fe_2O_3, the coordination numbers are not. In bulk Fe_2O_3, Fe has 3 Fe−O bonds at 1.944 Å and 3 bonds at 2.114 Å. In contrast, 10 Fe/Al_2O_3 has 3.9 Fe−O bonds at 1.93 Å and 1.6 Fe−O bonds at 2.11 Å. As EXAFS is a bulk average technique, these numbers likely reflect a mixture of different Fe−O coordination environments. Given the trend of the XANES showing a gradual increase in Fe−Fe orbital hybridization, the simplest explanation is that the 10 Fe/Al_2O_3 contains a mixture of Fe single sites, which have a Fe−O coordination number below 6, and small oligomeric Fe_2O_3 species that are 6 coordinate with oxygen. The presence of crystalline α-Fe_2O_3 was further ruled out via *ex situ* Raman measurements shown in Figure S21.

3.4. H_2 Temperature-Programmed Reduction (H_2-TPR) Experiments. It is known that the reduction behavior of a supported Fe species changes depending on its dispersion, size, and metal−support interaction.[57−59] Al_2O_3 was utilized as a control, and it showed a negligible peak due to its strong metal−oxygen bonds. H_2-TPR profile of bulk iron metal oxide is shown in Figure 5a. For Fe_2O_3, at least two distinct peaks

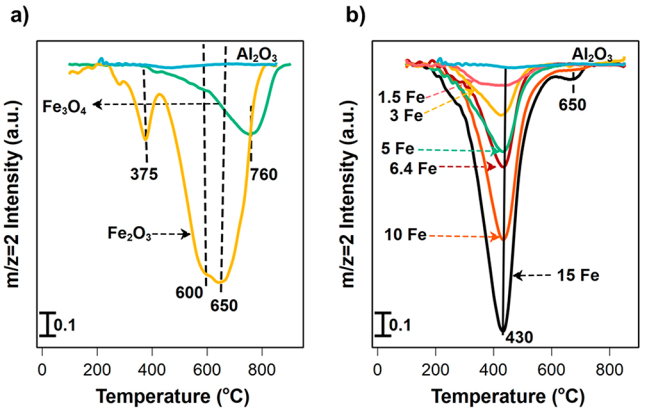

Figure 5. (a) Comparison of H_2-TPR profile of bulk Al_2O_3, iron oxide Fe_2O_3 and Fe_3O_4. (b) H_2-TPR profile of as-synthesized Fe/Al_2O_3 catalysts. Fe/Al_2O_3 represents catalyst after calcination in air at 600 °C for 4 h.

were observed at T = 375 and 650 °C. For bulk hematite (α-Fe_2O_3), a distinct peak at ~375 °C was assigned to $Fe_2O_3 \rightarrow Fe_3O_4$ reduction while the broad peak ~650 °C to $Fe_3O_4 \rightarrow FeO \rightarrow Fe$ reduction, similar to the reduction determined by *in situ* XRD.[60] For bulk magnetite (Fe_3O_4), one high-temperature broad peak with the highest peak intensity centered around ~760 °C was observed. The reduction of magnetite is expected to follow via $Fe_3O_4 \rightarrow FeO \rightarrow Fe$.[60] The multistep reduction generally causes broad reduction envelopes during the second and subsequent reduction step.[6,61]

To determine the reducibility of the as-synthesized catalysts, H_2-TPR experiments were carried out, and the corresponding plots are shown in Figure 5b. Only one broad peak with Tp_1 between 350 and 450 °C was observed for Fe/Al_2O_3 catalysts with no broad peak at T > 450 °C, indicating that the catalysts do not possess bulk-like Fe_2O_3 or Fe_3O_4 crystals, consistent with XRD experiments shown in Figure S2. The low-temperature peak at ~430 °C can be associated with the reduction of surface Fe^{3+} species. The broad peak at 450−700 °C has previously been attributed to reduction of FeO and Fe_3O_4 to Fe metal.[6] For 15 Fe/Al_2O_3, a satellite peak at 650 °C was observed which may be due to the formation of a minority 3D-Fe_2O_3 species due to the higher coverage.[30,50,51] This is consistent with XAS results presented in section 3.3, which indicates some agglomeration at higher Fe loading. From Figure 5b, it is observed that the peak temperature (Tp) of the supported Fe oxide species appears to be relatively independent of Fe loading over Al_2O_3.

https://doi.org/10.1021/acsanm.1c01366
ACS Appl. Nano Mater. XXXX, XXX, XXX−XXX

The activated catalysts after H_2S pretreatment (Fe/Al_2O_3-S) were generated and analyzed *in situ* using H_2-TPR. Al_2O_3-S showed a reduction peak at 450 °C, ascribed to loss of surface sulfur species, as shown in Figure 6a.[43] The reduction peak of

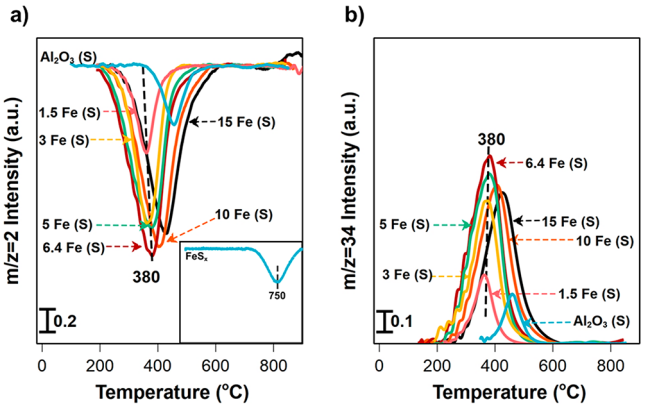

Figure 6. (a) H_2 consumption observed during H_2-TPR profile of various Fe loading (wt %) over Al_2O_3 after H_2S pretreatment. (b) H_2S evolution observed during H_2-TPR over various Fe loading (wt %) over Al_2O_3 after H_2S pretreatment. Fe (S) represents catalyst after H_2S pretreatment at 600 °C for 4 h. Inset represents H_2-TPR profile for reference FeS sample after H_2S pretreatment at 600 °C for 4 h.

bulk FeS, on the other hand, was observed at ~750 °C (Figure 6a inset).[62] In Figure 6a, a single reduction peak was observed during H_2-TPR for all the Fe/Al_2O_3-S catalysts. The peak at ~380 °C for 1.5−6.4 Fe/Al_2O_3-S catalysts shifted to a higher temperature for 10 and 15 Fe/Al_2O_3-S at 420 °C. The peak shift to a higher temperature for 10 and 15 Fe/Al_2O_3-S could be due to the formation of an extended structure on the surface of the catalyst. The peak around 380−430 °C can be attributed to the reduction of dispersed (available) iron sites. The lack of high-temperature peak evolution (~750 °C) indicates that Fe/Al_2O_3-S catalysts are free of bulk FeS nanoparticles on the surface. The lower H_2 consumption per gram of catalyst for H_2S pretreated samples as evinced by H_2-TPR is likely due to fromation of the conformal iron coating as indicated in the Figure 1. It is also plausible that iron species undergo reduction duirng H_2S pretreatment. It was observed that H_2 consumption during H_2-TPR, as observed in Figure 6a, leads to the formation of the H_2S for all catalysts, as shown in Figure 6b at the same peak temperature. It suggests that the Fe surface species reduction proceeded via $Fe\text{-}S + H_2 \rightarrow Fe + H_2S$, which indicates that the FeS_x species are present on the surface after H_2S pretreatment. These results suggest that after H_2S pretreatment, oxygen neighbor to Fe species is replaced by a sulfur atom.

In Table 2, the mmole of H_2 consumed per gram of catalyst is reported. It can be seen that increasing Fe loading up to 6.4 wt % resulted in an increasing amount of H_2 consumed. Interestingly, it was observed that the amount of H_2 consumed increases on as-synthesized catalyst but remains constant at ~0.46 mmol g^{-1} after 6.4 wt % Fe loading in H_2S pretreated. It indicates that increasing Fe loading above 6.4 wt % does not increase the number of reducible FeS_x species. These results are consistent with the presence of a conformal coating of the Fe species on the alumina, over the entire range of loadings. The Fe species remain bound to the alumina and do not form a separate phase. This is why the number of reducible Fe sites do not increase as the loading exceeds the monolayer capacity

Table 2. H_2 Consumed in Millimole per Gram of Catalyst As Obtained from H_2-TPR

	H_2, mmole consumed per gram of catalyst (H_2 consumed per mole of Fe atoms)	
Fe (wt %)	as synthesized	H_2S pretreated
0		0.12
1.5	0.24 (0.89)	0.23 (0.87)
3	0.32 (0.59)	0.32 (0.6)
5	0.45 (0.49)	0.42 (0.46)
6.4	0.54 (0.47)	0.46 (0.4)
10	0.77 (0.42)	0.46 (0.26)
15	1.12 (0.42)	0.44 (0.16)

of alumina for the sulfided Fe species (Figure 1). The monolayer capacity for the sulfided catalyst is reached at the 6.4 Fe catalyst loading.

3.5. Fixed Bed Catalytic PDH Studies for 10 Fe/Al_2O_3-H_2 and 10 Fe/Al_2O_3-S under Different H_2S Cofeed Conditions. The catalytic activity for PDH and selectivity toward C_3H_6 with time on stream (TOS) for 10 Fe/Al_2O_3-H_2 and 10 Fe/Al_2O_3-S catalysts in a fixed bed reactor are shown in Figure 7. The reaction rate, defined using eq 1, was measured in terms of moles of C_3H_8 consumed per gram of catalyst per second. The corresponding propane conversion is reported in Figure S22. The 10 Fe/Al_2O_3-H_2 shows an initial activity of ~1.1×10^{-7} mol g^{-1} s^{-1}, and the initial conversion was 5.6%. An induction period over 10 Fe/Al_2O_3-H_2 was observed, resulting in higher activity (2.69×10^{-7} mol g^{-1} s^{-1}, conversion = 13.5% at TOS −10 h) with TOS. The induction period of about 2 h before attaining steady-state for 10Fe/Al_2O_3-H_2 could be due to *in situ* formation of the iron carbide phase.[6] Previously, Tan et al.[6] showed that 10 Fe−P/Al_2O_3 could perform PDH with up to 82% C_3H_6 selectivity at 600 °C. They postulated that the *in situ* Fe_3C phase formation was responsible for high selectivity by comparing pre- and postreaction XRD. Recently, Wang and Senftle, based on electronic structure analyses, suggested that the high selectivity of Fe_3C originates from the disruption of surface ensembles via carbon species.[63]

Previously, Wang et al.[18] showed that supported metal oxides (such as Fe, Ni, Co. Mo, Mn, and Cu) upon H_2S pretreatment could perform selective i-C_4 dehydrogenation. Similarly, Sharma et al.[43] showed that H_2S pretreatment and cofeed could dramatically improve the catalytic performance of γ-Al_2O_3. Therefore, the effect of H_2S pretreatment and cofeed was studied for 10 Fe/Al_2O_3 and shown in Figure 7 and Figure S22. The maximum reaction rate (~1 μmol g^{-1} s^{-1}) and conversion (43.3%) for 10 Fe/Al_2O_3-S without H_2S cofeed were observed after 5 min of TOS. Afterward, it gradually decreased by ~60% at the end of 10 h cycle. The effect of different pretreatment conditions can be seen on both selectivity and activity. Notably, the activity is much higher upon H_2S pretreatment. Further, the propylene selectivity for the 10 Fe/Al_2O_3-S (>98%) catalyst was higher than the 10 Fe/Al_2O_3-H_2 (~96%). The increase in rate and selectivity of 10 Fe/Al_2O_3-S could be attributed to *in situ* sulfidation of 10 Fe/Al_2O_3 during H_2S pretreatment, as supported by the temperature program reduction results. The gradual decrease in the observed rate for 10 Fe/Al_2O_3-S was different from 10 Fe/Al_2O_3-H_2. The dramatic drop in activity for 10 Fe/Al_2O_3-S in the absence of H_2S cofeed could be due to loss of sulfur as

https://doi.org/10.1021/acsanm.1c01366
ACS Appl. Nano Mater. XXXX, XXX, XXX−XXX

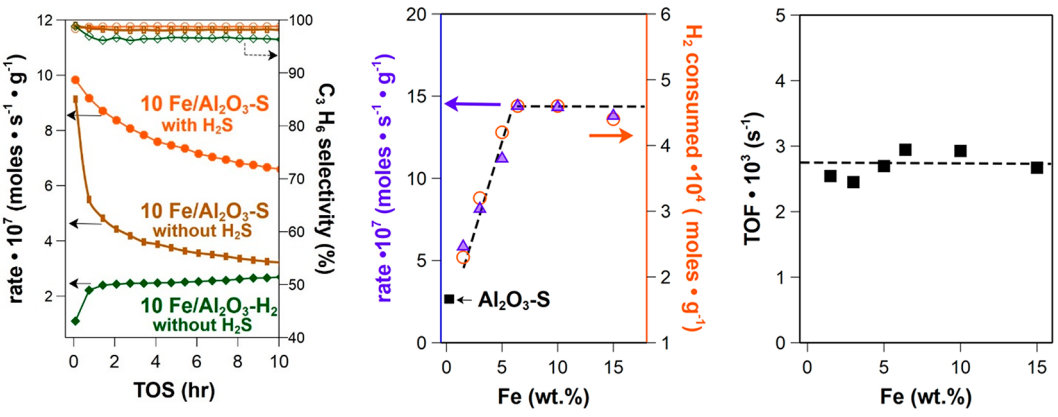

Figure 7. (a) Rate of C_3H_8 consumption and C_3H_6 selectivity for different pretreatments for 10 Fe/Al_2O_3. The feed contained 1.1% C_3H_8, 1% H_2, with (0.1%) and without H_2S cofeed, and the reaction temperature was 560 °C. The 10 Fe/Al_2O_3-H_2 catalyst was pretreated in 1% H_2 at 600 °C for 4 h. The 10 Fe/Al_2O_3-S catalyst was pretreated in 1% H_2S at 600 °C for 4 h. The total volumetric flow rate was 50 mL/min, and 200 mg of catalyst was used to achieve high conversion (~50%). Solid diamonds, squares, and octagon represent reaction rate, while empty diamonds, squares, and octagon represent C_3H_6 selectivity. (b) Rate of C_3H_8 and H_2 consumption as a function of Fe loading wt % for Fe/Al_2O_3-S catalysts. (c) Turnover frequencies (TOF) for C_3H_8 dehydrogenation as a function of Fe loading wt %. The feed contained 1.05% C_3H_8, 1% H_2, 0.1% H_2S with the balance being N_2, and the reaction temperature was 560 °C. The total volumetric flow rate was 75 mL/min, and 30 mg of catalyst was used to achieve differential conversion (<8%). The catalysts were pretreated in a 1 mol % H_2S stream at 600 °C for 4 h. The initial rates at TOS = 5 min are reported in the figure. Dashed lines are a guide to the eye.

reported in other work.[18] We attribute the deactivation to loss of S and possible coke deposition.

Figure 7 also shows the effect of H_2S cofeed on PDH over the 10 Fe/Al_2O_3-S catalyst. The initial selectivity slightly improved from 97.8% in the absence of H_2S to 98.5% in the presence of H_2S cofeed. The deactivation in the presence of H_2S cofeed was also substantially lower. These results indicate that the presence of H_2S is necessary for catalytic stability, and the deactivation could be due to gradual loss of sulfur with time on stream resulting in loss of active sites or formation of an inactive phase.[18] Importantly, the bulk FeS is not active or possessed a very low rate (selectivity ~65%) compared to the supported Fe/Al_2O_3-S catalysts (Table S6). This is in line with Cheng et al.'s[20] observation where bulk MoS_2 was much less active than supported MoS_2 by a factor of 7 toward i-C_4H_8 dehydrogenation.

Several side reactions can occur at such high operating temperatures, such as coking, thermal cracking to CH_4 and C_2H_4, and hydrogenolysis (via *in situ* H_2 produced during dehydrogenation reaction) to crack C_3H_8 to CH_4, C_2H_6. Interestingly, only CH_4 and C_2H_4 were observed as the byproducts, indicating cracking is the primary side reaction in the presence of H_2S cofeed.[43] The thermal conversion was found to be low (<0.1%), and the values are provided for reference in Table S6.

To study the effect of Fe loading, the reaction conditions such as volumetric flow rate and catalyst mass were optimized to achieve differential conversion <8% (see Figure S23) and initial rates are plotted in Figure 7b. The high conversion data are also reported in Table S7. Figure 7b shows the dependence of the rate of C_3H_8 dehydrogenation (at 1.05% C_3H_8, 1% H_2, and 0.1% H_2S at 560 °C) as a function of Fe loading up to 15 wt %. The C_3H_6 selectivity for Fe/Al_2O_3-S catalysts was about 98.5 ± 0.5, reported in Table S7. A linear increase in the rate of C_3H_6 dehydrogenation was observed up to 6.4 wt % Fe loading, beyond which these rates are essentially independent of the Fe content.

According to previous structural studies, it is reported that the Fe at low loadings leads to highly dispersed iron species.[24,31,32] In contrast, at high loadings (above monolayer, i.e., 5 Fe atoms nm^{-2}), it can result in hematite-like aggregates.[30,50,51] As pointed out using XAS (section 3.3), the catalyst contains single Fe sites at low loading and can form a minority Fe_2O_3 nanoparticles at higher loading. The plateau in the activity at high loading is indicative of the formation of an inactive phase at high loadings, possibly due to the formation of conformal Fe coating. Furthermore, the bulk FeS was determined to be inactive toward propane dehydrogenation (see Table S6). Also, a similar selectivity was obtained for all Fe loadings, which indicates that similar sites are responsible for chemistry at all loadings (Tables S6 and S7). The H_2 consumption also increased linearly and remains constant at higher loading, i.e., >6.4 wt % Fe (shown in Table 2) after H_2S pretreatment. The constant rate and H_2 consumption at higher loading (>6.4 wt % Fe) reveal that increasing iron loading beyond monolayer capacity does not result in more active sites.

The C_3H_6 dehydrogenation rate normalized per H_2 molecule (TOF) was determined using H_2-TPR and is shown in Figure 7c. The TOF's invariance with Fe loading suggests that the dehydrogenation of C_3H_8 to C_3H_6 involves only dispersed Fe (FeS_x) site and the rate is dependent on the number of exposed Fe sites. This also indicates that the active sites are reducible by H_2-TPR and H_2 can selectively titrate the active sites. Importantly, it suggests that the aggregated iron species (such as Fe_2O_3, FeO_xS_y, FeS) are not as active as dispersed Fe sites. It is generally accepted that propane conversion to propylene can occur over an individual active site of noble metal/metal alloys (such as Pt or Pd) and is a structure-insensitive reaction, whereas large ensembles of active sites can also induce structure-sensitive side reactions.[1,64−67] It implies that the rate of PDH reaction strongly

https://doi.org/10.1021/acsanm.1c01366
ACS Appl. Nano Mater. XXXX, XXX, XXX−XXX

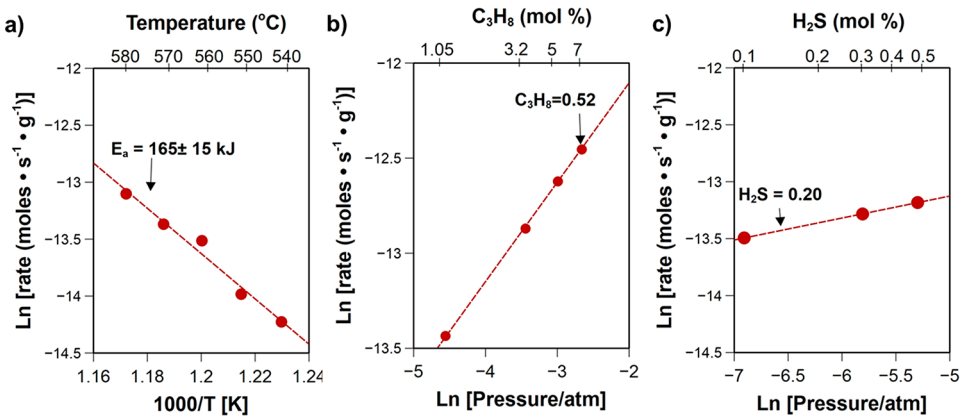

Figure 8. Observed kinetics of propane dehydrogenation reaction on 6.4 Fe/Al_2O_3-S. (a) Arrhenius plot (540−580 °C), with the feed containing 1.05% C_3H_8, 1% H_2, 0.1% H_2S with the balance being N_2. Partial pressure dependence of PDH kinetics on (b) propane (varied 1−7 mol %) and (c) H_2S (varied 0.1−0.5 mol %) is also shown. The reference concentrations of H_2 and H_2S were 1 and 0.1%, with the balance being N_2, such that the 30 mg of catalyst and total flow rate of 75 mL/min were ensured; the temperature was fixed at 560 °C to achieve differential conversion (<10%). The catalysts were pretreated in a 1 mol % H_2S stream at 600 °C for 4 h. The initial rates at TOS = 5 min are reported in the figure. The dashed lines are the linear fits to the data.

depends on the number of the active sites, and thus, the rate is directly proportional to the number of exposed atoms. Previously, Kim and Wachs studied vanadium oxide catalysts with different VO_x loading for selective methanol oxidation to formaldehyde.[68] It was reported in the study that the TOF on these catalysts is independent of the vanadium loading. Similar conclusions were reached for propane ODH over supported vanadium and chromium catalysts.[69−71] The constant TOF for propane consumption as a function of surface vanadia coverage indicates that only one surface VO_x site is involved in the rate-determining step of propane activation. The sum of these previous works suggests that a single surface site can perform selective propane dehydrogenation. In this study, similarly, a linear increase in rate up to 6.4 wt % Fe loading results from the increasing concentration of surface Fe sites. Similar selectivity and TOF at all loadings indicate that a single or dispersed site is required for the chemistry.

The kinetics of propane dehydrogenation was investigated on 6.4 Fe/Al_2O_3-S to determine apparent activation barriers and partial pressure dependence for propane in Figure 8. The C_3H_8 conversions of less than 12% are utilized in the temperature range between 540 and 580 °C for plotting the Arrhenius plot. The activation energy value determined was 165 kJ/mol in the temperature range from 540 to 580 °C. The apparent activation energy was similar to that obtained for Co- and Ru-based catalysts.[72,73] The reaction order for C_3H_8 was 0.52. A half order in propane for a single Fe site suggests reaction intermediates (or products) of the reaction, such as propyl or propylene, cover a significant fraction of sites and that either first or second C−H scission is rate determining. The corresponding selectivity and rate are plotted in Figure S24 for reference. Next, the effect of H_2S on the reaction kinetics was studied. The reaction order for H_2S was determined to be ∼0.20, indicating a promoting effect. It is likely that increasing H_2S concentration in the feed (or sulfur potential) leads to an increase in the number of available Fe sites. The reaction order of ∼0.20 for H_2S at either 560 or 600 °C (Figure S25) indicates that the effect of H_2S on kinetics is not strongly dependent on the reaction temperature. Of note, high selectivity can be maintained at high temperature and partial pressure of propane, showing the Fe/Al_2O_3-S catalyst potential for industrial applications.

Finally, summary of the catalytic data available in the literature for mixed or platinum group metal-free catalysts including Sn, Co, Fe, V, Ru for PDH is provided in Table S8. While direct comparison is difficult due to the variety of reaction temperatures, feed compositions, and H_2S pretreatment (if any), the best catalyst obtained in this work, 6.4 Fe/Al_2O_3-S, exhibited rates and TOF comparable to other nonprecious catalysts, chiefly used without H_2S cofeed. These catalysts can be partially or fully regenerated by a combination of H_2S or $H_2S + O_2$ treatments, as shown in the Figure S26.

4. CONCLUSIONS

A series of Fe loading (0−15 wt %) supported over Al_2O_3 catalysts were prepared via the incipient wetness impregnation method. XAS, AC-STEM, BET surface area confirm that the Fe remains atomically dispersed with no bulk nanophases detected. Additionally, EXAFS analysis showed that the second nearest neighbor of iron was aluminum, confirming the single-site nature of iron. Past monolayer coverage, the formation of iron oxide clusters as a minority species was suggested. H_2-TPR was utilized to study the reducibility of the catalyst in as-synthesized form and after H_2S pretreatment. In the oxide form, H_2-TPR scaled with loading, but H_2-TPR results on the sulfided catalyst indicate that the number of exposed Fe sites after H_2S pretreatment increases linearly up to 6.4 wt % and becomes constant at higher loading for H_2S pretreated samples. This result is explained by the Fe species remaining as a conformal coating on the alumina. Fe/Al_2O_3-S (pretreated with H_2S) showed improved performance compared to Fe/Al_2O_3-H_2; 52% propylene yield along with ∼99% C_3H_6 selectivity was obtained over 6.4 Fe/Al_2O_3-S. Like H_2-TPR, the reaction rate as a function of iron loading showed a plateau at higher loading, which corresponds to predicted monolayer coverage of sulfided Fe over Al_2O_3. At loadings above a monolayer, the number of sites does not increase because the Fe remains strongly bound to the alumina, without forming a separate phase. Importantly, it was determined that the TOF was constant irrespective of Fe loading, indicating that propane

https://doi.org/10.1021/acsanm.1c01366
ACS Appl. Nano Mater. XXXX, XXX, XXX−XXX

dehydrogenation rate is constant per Fe site. The constant TOF values demonstrate that the dispersed Fe site is responsible for the PDH reaction to propylene. The loss of sulfur and some coke deposition was believed to be the main reason for the deactivation of the catalyst since regeneration could be performed utilizing treatment in H_2S with and without oxygen to form the unique and reactive surface sites.

■ ASSOCIATED CONTENT

Supporting Information

The Supporting Information is available free of charge at https://pubs.acs.org/doi/10.1021/acsanm.1c01366.

Catalyst characterization such as TEM, XRD, PDF, EXAFS fitting; additional kinetic data such as conversion, rate, selectivity, and reaction orders at different reaction conditions (PDF)

■ AUTHOR INFORMATION

Corresponding Author

Jonas Baltrusaitis − *Department of Chemical and Biomolecular Engineering, Lehigh University, Bethlehem, Pennsylvania 18015, United States;* orcid.org/0000-0001-5634-955X; Email: job314@lehigh.edu

Authors

Lohit Sharma − *Department of Chemical and Biomolecular Engineering, Lehigh University, Bethlehem, Pennsylvania 18015, United States;* orcid.org/0000-0003-1405-1688

Stephen C. Purdy − *Neutron Scattering Division, Oak Ridge National Laboratory, Oak Ridge, Tennessee 37830, United States;* orcid.org/0000-0002-9870-1029

Katharine Page − *Neutron Scattering Division and Shull Wollan Center, Oak Ridge National Laboratory, Oak Ridge, Tennessee 37830, United States; Materials Science and Engineering Department, University of Tennessee, Knoxville, Tennessee 37996, United States;* orcid.org/0000-0002-9071-3383

Srinivas Rangarajan − *Department of Chemical and Biomolecular Engineering, Lehigh University, Bethlehem, Pennsylvania 18015, United States;* orcid.org/0000-0002-6777-9421

Hien Pham − *Center for Microengineered Materials and Department of Chemical & Biological Engineering, University of New Mexico, Albuquerque, New Mexico 87131, United States*

Abhaya Datye − *Center for Microengineered Materials and Department of Chemical & Biological Engineering, University of New Mexico, Albuquerque, New Mexico 87131, United States;* orcid.org/0000-0002-7126-8659

Complete contact information is available at: https://pubs.acs.org/10.1021/acsanm.1c01366

Author Contributions

L.S.: investigation (lead); conceptualization (supporting); writing of original draft (equal); manuscript review and editing (equal). S.C.P.: investigation (supporting); writing of original draft (equal); manuscript review and editing (equal). K.P.: investigation (supporting); writing of original draft (equal); manuscript review and editing (equal). S.R.: supervision (supporting); conceptualization (supporting); writing of original draft (equal); manuscript review and editing (equal). H.P.: investigation. A.D.: investigation; methodology; manuscript review and editing. J.B.: conceptualization (lead); methodology (supporting); funding acquisition; supervision (lead); writing of original draft (equal); manuscript review and editing (equal).

Notes

The authors declare no competing financial interest.

Data Availability. The data that support the findings of this study are available from the corresponding author upon request.

■ ACKNOWLEDGMENTS

This work is supported by the Center for Understanding and Control of Acid Gas-Induced Evolution of Materials for Energy (UNCAGE-ME), an Energy Frontier Research Center funded by the U.S. Department of Energy, Office of Science, Basic Energy Sciences under Grant DE-SC0012577. S.R. acknowledges support from the American Chemical Society Petroleum Research Fund (Grant 57946-DNI5). A.D. acknowledges support from the NSF/ERC CISTAR under Cooperative Agreement EEC-1647722 and for microscope acquisition under Grant DMR-1828731. MRCAT operations are supported by the Department of Energy and the MRCAT member institutions. This research used resources of the Advanced Photon Source, a U.S. Department of Energy (DOE) Office of Science User Facility operated for the DOE Offices of Science by Argonne National Laboratory under Contract DE-AC02-06CH11357. This research used resources at 28-ID-1 of the National Synchrotron Light Source II, a U.S. Department of Energy (DOE) Office of Science User Facility operated for the DOE Office of Science by Brookhaven National Laboratory under Contract DE-SC0012704.

■ REFERENCES

(1) Sattler, J. J. H. B.; Ruiz-Martinez, J.; Santillan-Jimenez, E.; Weckhuysen, B. M. Catalytic Dehydrogenation of Light Alkanes on Metals and Metal Oxides. *Chem. Rev.* **2014**, *114* (20), 10613−10653.

(2) Degnan, T. Commercial Catalytic Propane Dehydrogenation (PDH) Technology Offerings Broadened. *Focus Catal.* **2019**, *2019* (11), 1.

(3) Jiang, X.; Sharma, L.; Fung, V.; Park, S. J.; Jones, C. W.; Sumpter, B. G.; Baltrusaitis, J.; Wu, Z. Oxidative Dehydrogenation of Propane to Propylene with Soft Oxidants via Heterogeneous Catalysis. *ACS Catal.* **2021**, *11*, 2182−2234.

(4) Siirola, J. J. The Impact of Shale Gas in the Chemical Industry. *AIChE J.* **2014**, *60* (3), 810−819.

(5) Otroshchenko, T.; Jiang, G.; Kondratenko, V. A.; Rodemerck, U.; Kondratenko, E. V. Current Status and Perspectives in Oxidative, Non-Oxidative and CO2-Mediated Dehydrogenation of Propane and Isobutane over Metal Oxide Catalysts. *Chem. Soc. Rev.* **2021**, *50* (1), 473−527.

(6) Tan, S.; Hu, B.; Kim, W.-G.; Pang, S. H.; Moore, J. S.; Liu, Y.; Dixit, R. S.; Pendergast, J. G.; Sholl, D. S.; Nair, S.; Jones, C. W. Propane Dehydrogenation over Alumina-Supported Iron/Phosphorus Catalysts: Structural Evolution of Iron Species Leading to High Activity and Propylene Selectivity. *ACS Catal.* **2016**, *6* (9), 5673−5683.

(7) Schäferhans, J.; Gómez-Quero, S.; Andreeva, D. V.; Rothenberg, G. Novel and Effective Copper−Aluminum Propane Dehydrogenation Catalysts. *Chem. - Eur. J.* **2011**, *17* (44), 12254−12256.

(8) Hu, B.; Kim, W.-G.; Sulmonetti, T. P.; Sarazen, M. L.; Tan, S.; So, J.; Liu, Y.; Dixit, R. S.; Nair, S.; Jones, C. W. A Mesoporous Cobalt Aluminate Spinel Catalyst for Nonoxidative Propane Dehydrogenation. *ChemCatChem* **2017**, *9* (17), 3330−3337.

(9) Mitchell, P. C. H.; Wass, S. A. Propane Dehydrogenation over Molybdenum Hydrotalcite Catalysts. *Appl. Catal., A* **2002**, *225* (1), 153−165.
(10) Schweitzer, N. M.; Hu, B.; Das, U.; Kim, H.; Greeley, J.; Curtiss, L. A.; Stair, P. C.; Miller, J. T.; Hock, A. S. Propylene Hydrogenation and Propane Dehydrogenation by a Single-Site Zn2+ on Silica Catalyst. *ACS Catal.* **2014**, *4* (4), 1091−1098.
(11) Xiong, C.; Chen, S.; Yang, P.; Zha, S.; Zhao, Z.-J.; Gong, J. Structure−Performance Relationships for Propane Dehydrogenation over Aluminum Supported Vanadium Oxide. *ACS Catal.* **2019**, *9* (7), 5816−5827.
(12) Szeto, K. C.; Jones, Z. R.; Merle, N.; Rios, C.; Gallo, A.; Le Quemener, F.; Delevoye, L.; Gauvin, R. M.; Scott, S. L.; Taoufik, M. A Strong Support Effect in Selective Propane Dehydrogenation Catalyzed by Ga(i-Bu)3 Grafted onto γ-Alumina and Silica. *ACS Catal.* **2018**, *8* (8), 7566−7577.
(13) Wang, H.; Huang, H.; Bashir, K.; Li, C. Isolated Sn on Mesoporous Silica as a Highly Stable and Selective Catalyst for the Propane Dehydrogenation. *Appl. Catal., A* **2020**, *590*, 117291.
(14) Han, S.; Zhao, D.; Otroshchenko, T.; Lund, H.; Bentrup, U.; Kondratenko, V. A.; Rockstroh, N.; Bartling, S.; Doronkin, D. E.; Grunwaldt, J.-D.; Rodemerck, U.; Linke, D.; Gao, M.; Jiang, G.; Kondratenko, E. V. Elucidating the Nature of Active Sites and Fundamentals for Their Creation in Zn-Containing ZrO2-Based Catalysts for Nonoxidative Propane Dehydrogenation. *ACS Catal.* **2020**, *10* (15), 8933−8949.
(15) Zhang, Y.; Zhao, Y.; Otroshchenko, T.; Lund, H.; Pohl, M.-M.; Rodemerck, U.; Linke, D.; Jiao, H.; Jiang, G.; Kondratenko, E. V. Control of Coordinatively Unsaturated Zr Sites in ZrO2 for Efficient C−H Bond Activation. *Nat. Commun.* **2018**, *9* (1), 3794.
(16) Chen, S.; Chang, X.; Sun, G.; Zhang, T.; Xu, Y.; Wang, Y.; Pei, C.; Gong, J. Propane Dehydrogenation: Catalyst Development, New Chemistry, and Emerging Technologies. *Chem. Soc. Rev.* **2021**, *50*, 3315.
(17) Resasco, D. E.; Marcus, B. K.; Huang, C. S.; Durante, V. A. Isobutane Dehydrogenation over Sulfided Nickel Catalysts. *J. Catal.* **1994**, *146* (1), 40−55.
(18) Wang, G.; Li, C.; Shan, H. Highly Efficient Metal Sulfide Catalysts for Selective Dehydrogenation of Isobutane to Isobutene. *ACS Catal.* **2014**, *4* (4), 1139−1143.
(19) Wang, G.; Gao, C.; Zhu, X.; Sun, Y.; Li, C.; Shan, H. Isobutane Dehydrogenation over Metal (Fe, Co, and Ni) Oxide and Sulfide Catalysts: Reactivity and Reaction Mechanism. *ChemCatChem* **2014**, *6* (8), 2305−2314.
(20) Cheng, E.; McCullough, L.; Noh, H.; Farha, O.; Hupp, J.; Notestein, J. Isobutane Dehydrogenation over Bulk and Supported Molybdenum Sulfide Catalysts. *Ind. Eng. Chem. Res.* **2020**, *59* (3), 1113−1122.
(21) Bulánek, R.; Wichterlová, B.; Novoveská, K.; Kreibich, V. Oxidation of Propane with Oxygen and/or Nitrous Oxide over Fe-ZSM-5 with Low Iron Concentrations. *Appl. Catal., A* **2004**, *264* (1), 13−22.
(22) Kondratenko, E. V.; Pérez-Ramírez, J. Oxidative Functionalization of Propane over FeMFI Zeolites: Effect of Reaction Variables and Catalyst Constitution on the Mechanism and Performance. *Appl. Catal., A* **2004**, *267* (1), 181−189.
(23) Sarazen, M. L.; Jones, C. W. MOF-Derived Iron Catalysts for Nonoxidative Propane Dehydrogenation. *J. Phys. Chem. C* **2018**, *122* (50), 28637−28644.
(24) Hu, B.; Schweitzer, N. M.; Zhang, G.; Kraft, S. J.; Childers, D. J.; Lanci, M. P.; Miller, J. T.; Hock, A. S. Isolated FeII on Silica As a Selective Propane Dehydrogenation Catalyst. *ACS Catal.* **2015**, *5* (6), 3494−3503.
(25) Yun, J. H.; Lobo, R. F. Catalytic Dehydrogenation of Propane over Iron-Silicate Zeolites. *J. Catal.* **2014**, *312*, 263−270.
(26) Sun, Y.; Wu, Y.; Tao, L.; Shan, H.; Wang, G.; Li, C. Effect of Pre-Reduction on the Performance of Fe2O3/Al2O3 Catalysts in Dehydrogenation of Propane. *J. Mol. Catal. A: Chem.* **2015**, *397*, 120−126.
(27) Sun, Y.; Wu, Y.; Shan, H.; Wang, G.; Li, C. Studies on the Promoting Effect of Sulfate Species in Catalytic Dehydrogenation of Propane over Fe2O3/Al2O3 Catalysts. *Catal. Sci. Technol.* **2015**, *5* (2), 1290−1298.
(28) Watanabe, R.; Hirata, N.; Miura, K.; Yoda, Y.; Fushimi, Y.; Fukuhara, C. Formation of Active Species for Propane Dehydrogenation with Hydrogen Sulfide Co-Feeding over Transition Metal Catalyst. *Appl. Catal., A* **2019**, *587*, 117238.
(29) Watanabe, R.; Hirata, N.; Fukuhara, C. Active Species of Sulfated Metal Oxide Catalyst for Propane Dehydrogenation. *J. Jpn. Pet. Inst.* **2017**, *60* (5), 223−231.
(30) Tomita, A.; Miki, T.; Tango, T.; Murakami, T.; Nakagawa, H.; Tai, Y. Fe K-Edge X-Ray Absorption Fine Structure Determination of γ-Al2O3-Supported Iron-Oxide Species. *ChemPhysChem* **2015**, *16* (9), 2015−2020.
(31) Brandenberger, S.; Kröcher, O.; Tissler, A.; Althoff, R. The Determination of the Activities of Different Iron Species in Fe-ZSM-5 for SCR of NO by NH3. *Appl. Catal., B* **2010**, *95* (3), 348−357.
(32) Høj, M.; Beier, M. J.; Grunwaldt, J.-D.; Dahl, S. The Role of Monomeric Iron during the Selective Catalytic Reduction of NOx by NH3 over Fe-BEA Zeolite Catalysts. *Appl. Catal., B* **2009**, *93* (1), 166−176.
(33) Brandenberger, S.; Kröcher, O.; Tissler, A.; Althoff, R. The State of the Art in Selective Catalytic Reduction of NOx by Ammonia Using Metal-Exchanged Zeolite Catalysts. *Catal. Rev.: Sci. Eng.* **2008**, *50* (4), 492−531.
(34) Sharma, L.; Brigaityte, O.; Honer, K.; Kalfaoglu, E.; Slinksiene, R.; Streimikis, V.; Sviklas, A. M.; Baltrusaitis, J. Carnallite-Derived Solid Waste as Potassium (K) and Magnesium (Mg) Source in Granulated Compound NPK Fertilizers. *ACS Sustainable Chem. Eng.* **2018**, *6* (7), 9427−9433.
(35) Barrett, E. P.; Joyner, L. G.; Halenda, P. P. The Determination of Pore Volume and Area Distributions in Porous Substances. I. Computations from Nitrogen Isotherms. *J. Am. Chem. Soc.* **1951**, *73* (1), 373−380.
(36) Prescher, C.; Prakapenka, V. B. DIOPTAS: A Program for Reduction of Two-Dimensional X-Ray Diffraction Data and Data Exploration. *High Pressure Res.* **2015**, *35* (3), 223−230.
(37) Juhás, P.; Davis, T.; Farrow, C. L.; Billinge, S. J. L. PDFgetX3: A Rapid and Highly Automatable Program for Processing Powder Diffraction Data into Total Scattering Pair Distribution Functions. *J. Appl. Crystallogr.* **2013**, *46* (2), 560−566.
(38) Farrow, C. L.; Juhas, P.; Liu, J. W.; Bryndin, D.; Bozin, E. S.; Bloch, J.; Proffen, T.; Billinge, S. J. L. PDFfit2 and PDFgui: Computer Programs for Studying Nanostructure in Crystals. *J. Phys.: Condens. Matter* **2007**, *19* (33), 335219.
(39) Kropf, A. J.; Katsoudas, J.; Chattopadhyay, S.; Shibata, T.; Lang, E. A.; Zyryanov, V. N.; Ravel, B.; McIvor, K.; Kemner, K. M.; Scheckel, K. G.; Bare, S. R.; Terry, J.; Kelly, S. D.; Bunker, B. A.; Segre, C. U. The New MRCAT (Sector 10) Bending Magnet Beamline at the Advanced Photon Source. *AIP Conf. Proc.* **2009**, *1234* (1), 299−302.
(40) Kraft, S.; Stümpel, J.; Becker, P.; Kuetgens, U. High Resolution X-Ray Absorption Spectroscopy with Absolute Energy Calibration for the Determination of Absorption Edge Energies. *Rev. Sci. Instrum.* **1996**, *67* (3), 681−687.
(41) Haskel, D. FLUO: Correcting XANES for Self-Absorption in Fluorescence Measurements. University of Washington: Seattle, WA, 1999.
(42) Kiani, D.; Sourav, S.; Wachs, I. E.; Baltrusaitis, J. Synthesis and Molecular Structure of Model Silica-Supported Tungsten Oxide Catalysts for Oxidative Coupling of Methane (OCM). *Catal. Sci. Technol.* **2020**, *10* (10), 3334−3345.
(43) Sharma, L.; Jiang, X.; Wu, Z.; Baltrus, J.; Rangarajan, S.; Baltrusaitis, J. Elucidating the Origin of Selective Dehydrogenation of Propane on γ-Alumina under H2S Treatment and Co-Feed. *J. Catal.* **2021**, *394*, 142−156.
(44) Sharma, L.; Upadhyay, R.; Rangarajan, S.; Baltrusaitis, J. Inhibitor, Co-Catalyst, or Co-Reactant? Probing the Different Roles

https://doi.org/10.1021/acsanm.1c01366
ACS Appl. Nano Mater. XXXX, XXX, XXX−XXX

of H2S during CO2 Hydrogenation on the MoS2 Catalyst. *ACS Catal.* **2019**, *9* (11), 10044−10059.
(45) Tischler, L. G.; Wing, M. S.. Process for Dehydrogenation of Propane. U.S. Patent 3,773,850, 1973.
(46) Xiong, H.; Lin, S.; Goetze, J.; Pletcher, P.; Guo, H.; Kovarik, L.; Artyushkova, K.; Weckhuysen, B. M.; Datye, A. K. Thermally Stable and Regenerable Platinum−Tin Clusters for Propane Dehydrogenation Prepared by Atom Trapping on Ceria. *Angew. Chem.* **2017**, *129*, 9114−9119.
(47) Thommes, M.; Kaneko, K.; Neimark, A. V.; Olivier, J. P.; Rodriguez-Reinoso, F.; Rouquerol, J.; Sing, K. S. W. Physisorption of Gases, with Special Reference to the Evaluation of Surface Area and Pore Size Distribution (IUPAC Technical Report). *Pure Appl. Chem.* **2015**, *87* (9−10), 1051−1069.
(48) Rudolph, M.; Motylenko, M.; Rafaja, D. Structure Model of γ-Al2O3 Based on Planar Defects. *IUCrJ* **2019**, *6*, 116−127.
(49) Yan, W.; Luo, J.; Kouk, Q.-Y.; Zheng, J.; Zhong, Z.; Liu, Y.; Borgna, A. Improving Oxidative Dehydrogenation of 1-Butene to 1,3-Butadiene on Al2O3 by Fe2O3 Using CO2 as Soft Oxidant. *Appl. Catal., A* **2015**, *508*, 61−67.
(50) Xie, Y.; Xu, X.; Zhao, B.; Tang, Y.; Wu, G. Studies on the Dispersion States of Fe2O3 on γ-Al2O3 by Means of Mössbauer Spectroscopy and XRD. *Catal. Lett.* **1992**, *13* (3), 239−245.
(51) Hoffmann, D. P.; Houalla, M.; Proctor, A.; Fay, M. J.; Hercules, D. M. Quantitative Characterization of Fe/Al2O3 Catalysts. Part I: Oxidic Precursors. *Appl. Spectrosc.* **1992**, *46* (2), 208−218.
(52) Botta, P. M.; Aglietti, E. F.; Porto López, J. M. Mechanochemical Synthesis of Hercynite. *Mater. Chem. Phys.* **2002**, *76* (1), 104−109.
(53) Lee, H.-Y.; Pack, Y.-K.; Lee, B.-K.; Kang, S.-J. L. Discontinuous Dissolution of Iron Aluminate Spinel in the Al2O3−Fe2O3 System. *J. Am. Ceram. Soc.* **1995**, *78* (8), 2149−2152.
(54) Hoffmann, D. P.; Houalla, M.; Proctor, A.; Hercules, D. M. Quantitative Characterization of Fe/Al2O3 Catalysts. Part II: Reduction, Sulfidation, and CO/Hydrogenation Activity. *Appl. Spectrosc.* **1992**, *46* (3), 489−497.
(55) Yang, M.; You, F. Comparative Techno-Economic and Environmental Analysis of Ethylene and Propylene Manufacturing from Wet Shale Gas and Naphtha. *Ind. Eng. Chem. Res.* **2017**, *56* (14), 4038−4051.
(56) Ayyub, P.; Palkar, V. R.; Chattopadhyay, S.; Multani, M. Effect of Crystal Size Reduction on Lattice Symmetry and Cooperative Properties. *Phys. Rev. B: Condens. Matter Mater. Phys.* **1995**, *51* (9), 6135−6138.
(57) Cagnoli, M. V.; Marchetti, S. G.; Gallegos, N. G.; Alvarez, A. M.; Mercader, R. C.; Yeramian, A. A. Influence of the Support on the Activity and Selectivity of High Dispersion Fe Catalysts in the Fischer−Tropsch Reaction. *J. Catal.* **1990**, *123* (1), 21−30.
(58) Park, J.-Y.; Lee, Y.-J.; Khanna, P. K.; Jun, K.-W.; Bae, J. W.; Kim, Y. H. Alumina-Supported Iron Oxide Nanoparticles as Fischer−Tropsch Catalysts: Effect of Particle Size of Iron Oxide. *J. Mol. Catal. A: Chem.* **2010**, *323* (1), 84−90.
(59) Wan, H.; Wu, B.; Xiang, H.; Li, Y. Fischer−Tropsch Synthesis: Influence of Support Incorporation Manner on Metal Dispersion, Metal−Support Interaction, and Activities of Iron Catalysts. *ACS Catal.* **2012**, *2* (9), 1877−1883.
(60) Jozwiak, W. K.; Kaczmarek, E.; Maniecki, T. P.; Ignaczak, W.; Maniukiewicz, W. Reduction Behavior of Iron Oxides in Hydrogen and Carbon Monoxide Atmospheres. *Appl. Catal., A* **2007**, *326* (1), 17−27.
(61) Ren-Yuan, T.; Su, Z.; Chengyu, W.; Dongbai, L.; Liwu, L. An in Situ Combined Temperature-Programmed Reduction-Mössbauer Spectroscopy of Alumina-Supported Iron Catalysts. *J. Catal.* **1987**, *106* (2), 440−448.
(62) Li, H.; Liu, J.; Li, J.; Hu, Y.; Wang, W.; Yuan, D.; Wang, Y.; Yang, T.; Li, L.; Sun, H.; Ren, S.; Zhu, X.; Guo, Q.; Wen, X.; Li, Y.; Shen, B. Promotion of the Inactive Iron Sulfide to an Efficient Hydrodesulfurization Catalyst. *ACS Catal.* **2017**, *7* (7), 4805−4816.
(63) Wang, P.; Senftle, T. P. Theoretical Insights into Non-Oxidative Propane Dehydrogenation over Fe3C. *Phys. Chem. Chem. Phys.* **2021**, *23* (2), 1401−1413.
(64) Childers, D. J.; Schweitzer, N. M.; Shahari, S. M. K.; Rioux, R. M.; Miller, J. T.; Meyer, R. J. Modifying Structure-Sensitive Reactions by Addition of Zn to Pd. *J. Catal.* **2014**, *318*, 75−84.
(65) Purdy, S. C.; Seemakurthi, R. R.; Mitchell, G. M.; Davidson, M.; Lauderback, B. A.; Deshpande, S.; Wu, Z.; Wegener, E. C.; Greeley, J.; Miller, J. T. Structural Trends in the Dehydrogenation Selectivity of Palladium Alloys. *Chem. Sci.* **2020**, *11* (19), 5066−5081.
(66) Cortright, R. D.; Goddard, S. A.; Rekoske, J. E.; Dumesic, J. A. Kinetic Study of Ethylene Hydrogenation. *J. Catal.* **1991**, *127* (1), 342−353.
(67) Chen, S.; Pei, C.; Sun, G.; Zhao, Z.-J.; Gong, J. Nanostructured Catalysts toward Efficient Propane Dehydrogenation. *Accounts Mater. Res.* **2020**, *1* (1), 30−40.
(68) Kim, T.; Wachs, I. E. CH3OH Oxidation over Well-Defined Supported V2O5/Al2O3 Catalysts: Influence of Vanadium Oxide Loading and Surface Vanadium−Oxygen Functionalities. *J. Catal.* **2008**, *255* (2), 197−205.
(69) Carrero, C. A.; Schloegl, R.; Wachs, I. E.; Schomaecker, R. Critical Literature Review of the Kinetics for the Oxidative Dehydrogenation of Propane over Well-Defined Supported Vanadium Oxide Catalysts. *ACS Catal.* **2014**, *4* (10), 3357−3380.
(70) Grant, J. T.; Carrero, C. A.; Love, A. M.; Verel, R.; Hermans, I. Enhanced Two-Dimensional Dispersion of Group V Metal Oxides on Silica. *ACS Catal.* **2015**, *5* (10), 5787−5793.
(71) Cherian, M.; Rao, M. S.; Hirt, A. M.; Wachs, I. E.; Deo, G. Oxidative Dehydrogenation of Propane over Supported Chromia Catalysts: Influence of Oxide Supports and Chromia Loading. *J. Catal.* **2002**, *211* (2), 482−495.
(72) Dai, Y.; Gu, J.; Tian, S.; Wu, Y.; Chen, J.; Li, F.; Du, Y.; Peng, L.; Ding, W.; Yang, Y. γ-Al2O3 Sheet-Stabilized Isolate Co2+ for Catalytic Propane Dehydrogenation. *J. Catal.* **2020**, *381*, 482−492.
(73) Otroshchenko, T.; Kondratenko, V. A.; Rodemerck, U.; Linke, D.; Kondratenko, E. V. ZrO2-Based Unconventional Catalysts for Non-Oxidative Propane Dehydrogenation: Factors Determining Catalytic Activity. *J. Catal.* **2017**, *348*, 282−290.

https://doi.org/10.1021/acsanm.1c01366
ACS Appl. Nano Mater. XXXX, XXX, XXX−XXX